Supporting Information

Polymer Modulated Ink Rheology and Compatibility Enables Homogenization Printing of Spiro-OMeTAD Transport Layer for Scalable and Stable Perovskite Solar Modules

Jin Li, Baojing Fan, Xukai Liu, Yuxin Liu, Zhi Xing, Chenxiang Gong, Zhaoyang Chu, Linfeng Li, Xiangchuan Meng, Rui Guo*, Fuyi Wang, Xiaotian Hu*, Yiwang Chen*

Experimental Section/Methods

Materials: All chemicals and reagents are directly purchased and used without further optimization or purification, including anhydrous N, N- dimethylformamide (DMF, purity 99.8%, Sigma-Aldrich with molecular sieve), anhydrous dimethyl sulfoxide (DMSO, purity 99.9%, Sigma-Aldrich with molecular sieve) and acetonitrile (purity 99.8%, Sigma-Aldrich with molecular sieve), chlorobenzene (CB, purity 99.8%, Sigma-Aldrich), methylammonium iodide (FAI, Xi'an Yuri Solar Co., Ltd.), methane bromide (MABr, Xi'an Yuri Solar Co., Ltd.), methylammonium chloride (MACl, Xi'an Yuri Solar Co., Ltd.), cesium iodide (CsI, Xi'an Yuri Solar Co., Ltd.), lead (II) iodide (PbI_2. 15% H_2O colloidal dispersion, Alfa Asear), lithium bis (trifluoromethylsulfonyl) imide (Li-TFSI, 98% purity, Alfa Asear), 2,2', 7,7'-tetrakis [n, n-di (4-methoxyphenyl) amino]- 9'-spirobifluorene (Spiro-OMeTAD, 99% purity, luminosity technology crop), Poly(4-vinylpyridine) (Macklin, average Mw~60000 andMw~160000, HANGZHOU XINQIAO BIOTECHNOLOGY CO.LTD, **M_W~10000**), 4-tert-butylpyridine (tBP, Sigma-Aldrich)、ChloroformChloroform(Sigma-Aldrich), Silver (Ag) was purchased from commercial sources with high purity (≥99.999%).

Preparation of Perovskite Precursor Solutions: The perovskite precursor solution ($Cs_{0.05}FA_{0.85}MA_{0.1}Pb(I_{0.97}Br_{0.03})_3$) was prepared by dissolving a mixture of CsI (19.8 mg), MACl (20.3 mg), MABr (16.2 mg), PbI2 (742.2 mg), FAI (224.4 mg), and in 1 mL anhydrous DMF/DMSO mixture solvent (4/1, v/v). For water-oxygen sensitive $FAPbI_3$, 1.5 M $FAPbI_3$ as well as 30% MACl were added into 1 mL anhydrous DMF/NMP mixture solvent (4/1, v/v)

Preparation of Carrier Transport Layer Solutions: The Spiro-OMeTAD solution was prepared by adding 90 mg Spiro-OMeTAD, different percentage content of P4VP, 4-tertbutylpyridine 35 μL, Li-TFSI acetonitrile solution 21 μL (520 mg Li-TFSI is dissolved in 1 ml acetonitrile) in 1mL chloroform. The SnO_2 precursor was prepared by mixing the SnO_2 colloidal solution with DI water by a ratio of 1:3 and then add KCl in it (1 mg/ml).

Device fabrication: ITO-coated glass substrates were cleaned in an ultrasonic bath containing acetone, deionized (DI) water, and ethanol for 20 min in each step and then dried with a nitrogen (N_2) stream followed by air plasma treatment for 10 min. For small-sized perovskite solar cell devices, the electron transport layer, perovskite light absorption layer and hole transport layer are all prepared by meniscus printing with triplet in low humidity (about 10%RH) environment. To prepare the SnO_2 electron transport layer, the blade speed is 5 mm s^{-1}, the distance between the meniscus and the substrate is 50 μm, and the substrate heating temperature is 50 °C. Then the obtained substrate coated with SnO_2 is annealed at 150 °C for 30 minutes under low humidity. For the preparation of perovskite light-absorbing layer, the perovskite precursor solution was coated on the electron transport layer substrate by meniscus printing, the blade speed is 5 mm s^{-1}, and the distance between the scraper and the substrate was 100 μm. Before film annealing, vacuum pretreatment (vacuum degree less than 20 Pa for 3 min) is needed. Then, the perovskite precursor coated substrate was annealed on a hot stage at 150 °C for 10 minutes. Subsequently, the Spiro-OMeTAD were deposited by meniscus coating continuously. After drying, the common electrode was scraped off, and then the Ag contact electrode with a thickness of 100 nm was evaporated under a high vacuum level of 3.5×10^{-4} Pa.

Fabrication of Perovskite Solar Modules: The fabrication process of perovskite solar modules (PSMs) and their environment condition were identical to that of small-area optoelectronic devices, but their effective areas were different. The 25 cm^2 solar module consisted of 7 sub-cells and the size of a single cell is 2.42 cm^2, so the effective area is 16.9 cm^2; similarly, the 100 cm^2 solar module consisted of 10 sub-cells and the size of a single cell is 6.57 cm^2, so the effective area is 65.9 cm^2. All scribing techniques were performed by the rectification unit, the dislocation of Ag and ITO is about 0.25 cm. No further encapsulation was performed on PSCs and PSMs.

Film Characterizations: The morphology of films was measured by AFM (nanoscope multimode Bruker) and SEM (JEOL, JSM-7500F, 104 Japan) at an accelerating voltage of 5.0 KV. TRPL excitation energy flow from 405 pulsed laser with wavelength of 405±8nm, pulse width of 45 ps and repetition rate of 0.1 MHz is about 4 nj cm^{-2}. PL attenuation data were recorded by time-dependent single photon counting technique (FLS920, Edinburgh Instruments Ltd.). FTIR spectra were recorded on Shimadzu IR Prestige-21 spectrometer.

Characterization of Solar Cells: The current density–voltage (*J–V*) and current-voltage (*I–V*) curves were characterized by using Keithley 2400 Source meter in glove box (N_2 atmosphere). The illuminated currents were measured under the solar simulated (Enli-Tech, 100 mW cm^{-2} and AM 1.5 G irradiation). The forward scan range is from 0 to 1200 mV and the RS range is from 1200 mV to 0 mV, with 2.0 mV for each step.

The scan rate is 200 mV s^{-1} and the delay time is 30 ms. The incident photon-to-current conversion efficiency (IPCE) spectra were detected in glove box (N_2 atmosphere) under monochromatic illumination (Oriel Cornerstone 260 1/4 m monochromator equipped with Oriel 70613NS QTH lamp), and the calibration of the incident light was performed with a monocrystalline silicon diode. The EIS was performed in low humidity environment (<10%RH) with Zahner electrochemical workstation in the dark from 0.1 to 106 Hz with 50 mV amplitude and the DC bias was kept at 750 mV. For the humidity stability of solar cells, the unsealed devices were stored in the dark at about 30 °C and about 50%RH, and the PCE of the devices related to the storage time was monitored. For thermal stability, the unpackaged devices were monitored at about 75-80 °C in a nitrogen (N_2) atmosphere.

High Performance Liquid Chromatography (HPLC): The instrument model is Agilent 1290. A Supersil ODS2 C18 (4.6×250 mm, 5 μm) column is applied at 25 °C. The inlet volume of the testing process is 2 μL, the detection wavelength is UV 260nm, and the gradient elution is carried out using water and acetonitrile as mobile phases.

TOF-SIMS: The dual-beam TOF-SIMS depth profiling characterizations are obtained on a TOF-SIMS 5 instrument (IONTOF GmbH) in an interlaced mode. For the detection of anions, a pulsed 30 keV Bi_3^+ ion beam was used as the analysis beam with the beam current of 0.55 pA. The analysis area was 100 × 100 $μm^2$ that was at the center of the sputter crater of 300 × 300 $μm^2$. A 20 keV argon gas cluster ion beam was used as the sputter beam with the beam current adjusted to be ~11 nA.

For the detection of anions, a 30 KeV Bi_3^+ ion beam was used as the analyzing source with beam current of 0.55 pA and analyzing area 100×100 um^2. A 20 KeV Ar^+ ion beam was used as the sputtering source with current ~10.5 nA and sputtering area 300×300 um^2.

Computational Method: First, pretreatment and structural optimization are executed on the structure of P4VP and Spiro-OMeTAD, and then conformation search and matching are executed on their structures to find the most possible combination mode. Combined with the evaluation and analysis of the docking results, the possible combination modes are finally obtained and optimized as necessary. The principle of this calculation is based on the physicochemical or biochemical interactions such as intermolecular affinity, hydrophobic interactions, electrostatic interactions, hydrogen bonding and other interactions. By calculating the energy and geometric matching arising from these interactions, the combination mode of the two structures can be predicted, and the possible potential binding sites and selectivity can be also inferred.

To explore the interactions between P4VP and Spiro-OMeTAD molecules, we performed 20 ps molecular dynamic simulation with using GFN0-xTB method in xtb software.[1] The interval for trajectory printout was set to 50 fs. The temperature and time step were set to 298.15 K and 1 fs, respectively. The mass of hydrogen atoms was set to 1 time. We use SHAKE algorithm to constrain X-H bonds. Under this scenario, we could obtain 400 dimers. Then, we used Molclus software [2] to invoke xtb to optimize all structures using GFN0-xTB method, followed by energy sorting and elimination of the 352 dimers. Further structural optimization was performed using the GFN2-xTB method. This was followed by energy sorting to select the six configurations with relative low energy for interaction analysis. The single point energy calculations of six dimers were performed by using B3LYP functional [3, 4] and 6-31G(d) basis set [5] in Gaussian 16 package. The Grimme's DFT-D3 with BJ-damping method was applied to correct the dispersion interaction. The independent gradient model based on Hirshfeld partition (IGMH) was a new method for visual study of interactions in chemical systems.[6] Thus, we used IGMH to study the interaction between different molecules with setting the isovalue is 0.005 a.u. The isosurface maps were rendered by means of Visual Molecular Dynamics (VMD) software [7] based on the files exported by Multiwfn.[8]

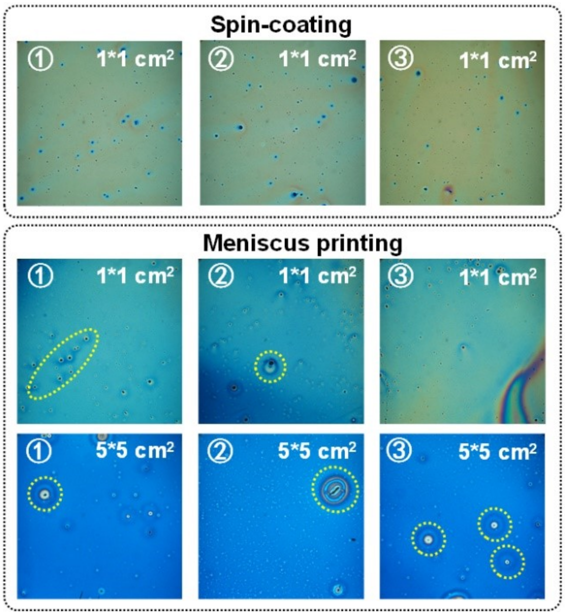

Supplementary Fig. 1 The optical microscope images of Spiro-OMeTAD obtained by spin coating and meniscus printing (The size is 1×1 cm^2, and 5×5 cm^2, respectively).

As shown in **Supplementary Fig. 1**, compared to the spin-coating process, the printed Spiro-OMeTAD suffers from inhomogeneous distribution as well as holes, and the extent of which worsens with the increase of size.

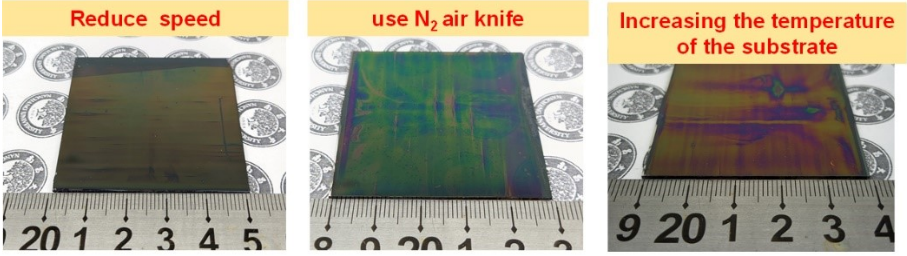

Supplementary Fig. 2 Photograph of Spiro-OMeTAD film printed on the meniscus, with the printed strips noted in the purple square.

As shown in **Supplementary Fig. 2**, it is also difficult to change the auxiliary process of printing to achieve homogeneous printing with good repeatability.

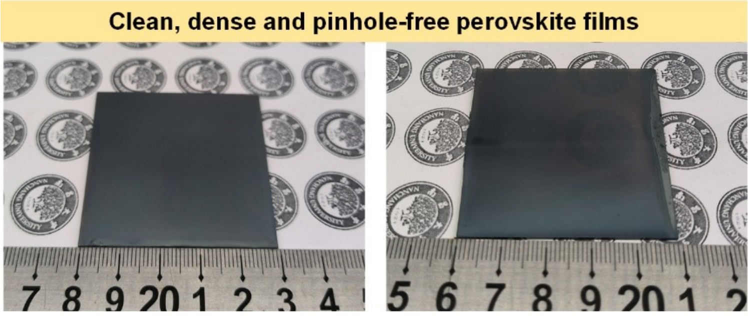

Supplementary Fig. 3 Photographs of bright, clean perovskite films obtained by meniscus printing.

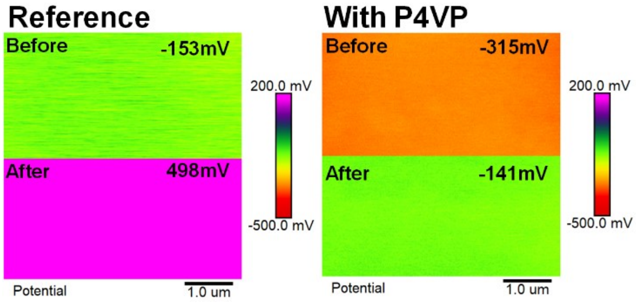

Supplementary Fig. 4 KPFM images of reference and P4VP sample before and after aging under ~75–85 °C in N_2 for 1000 h (The voltage is applied to the probe during the test).

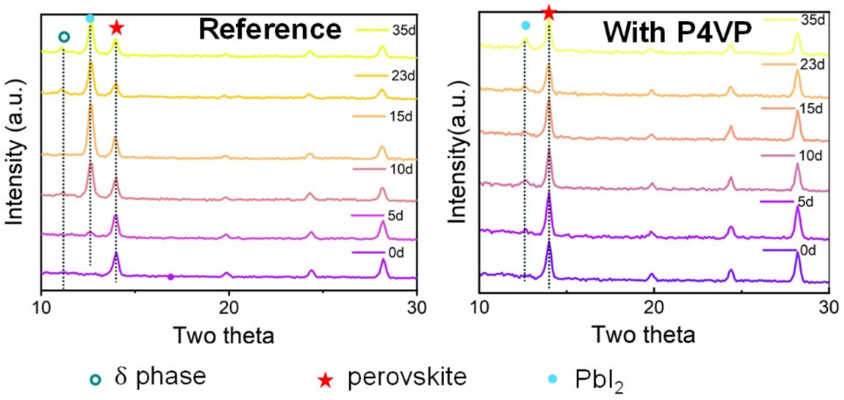

Supplementary Fig. 5 XRD evolution over time of rigid PSCs based on reference and doped with P4VP in Spiro-OMeTAD (50% RH, ~25–35 °C in air).

According to the XRD evolution diagram in **Supplementary Fig. 5**, the Spiro-OMeTAD of the reference sample cannot effectively protect the perovskite from water erosion in the air environment, but the crystal structure of the perovskite is well maintained after adding P4VP.

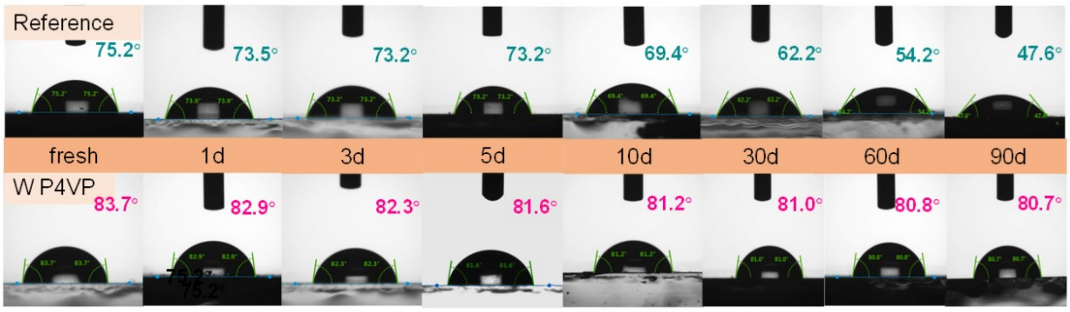

Supplementary Fig. 6 The water contact angles of Spiro-OMeTAD with or without P4VP at different aging times are in N_2 atmosphere.

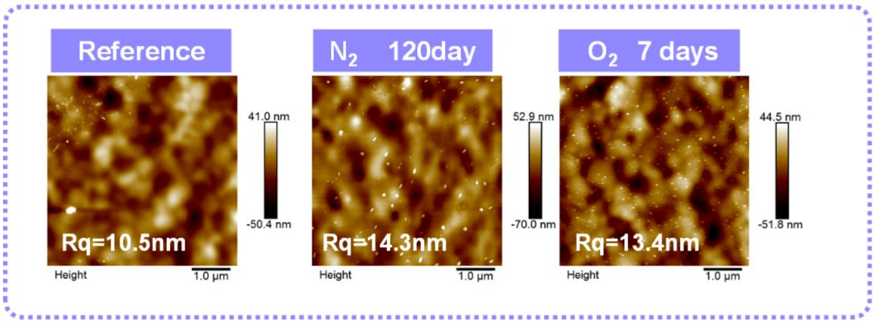

Supplementary Fig. 7 AFM morphology of Spiro-OMeTAD, a reference sample, stored in nitrogen for 120 days and oxidized in a drying cabinet for 7 days respectively.

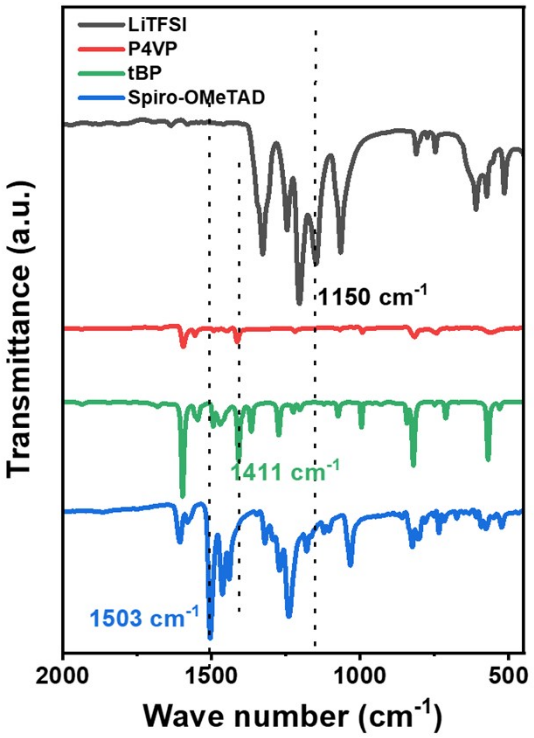

Supplementary Fig. 8 FTIR spectroscopy of pure LiTFSI, P4VP, tBP and Spiro-OMeTAD.

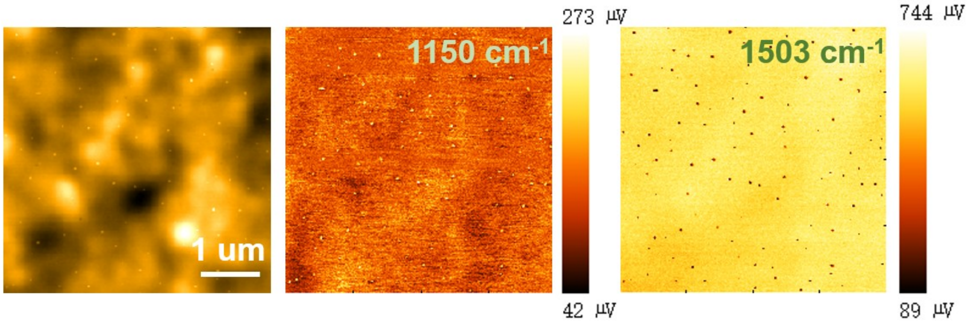

Supplementary Fig. 9 PiFM image of the printed reference Spiro-OMeTAD film in wavenumber of 1150 cm^{-1} and 1503 cm^{-1}.

Optical induced force microscopy (PiFM) is used to demonstrate that the small particles are LiTFSI. The characteristic wavenumber of LiTFSI is about 1150 cm^{-1}, and that of Spiro-OMeTAD is about 1503 cm^{-1} (Supplementary Fig. 8). The small particles show strong signals at 1150 cm^{-1} and at very low signals at 1370 cm^{-1}. Combined with the AFM analysis ahead, it can indicate that the precipitated particles are LiTFSI.

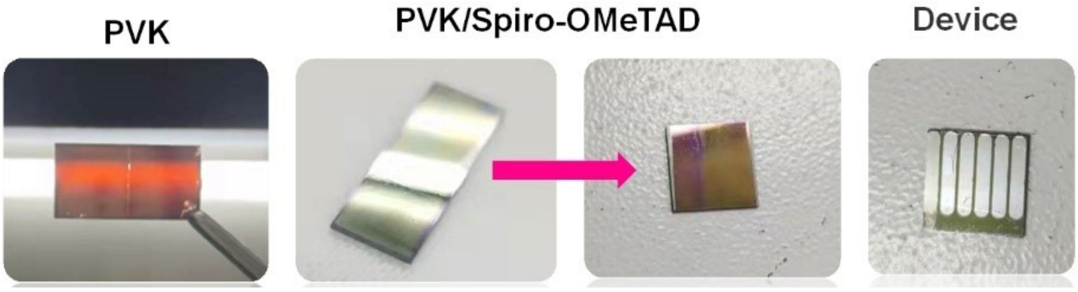

Supplementary Fig. 10 Display of fully-functional-layer printed devices (The effective area is 0.04 cm^2).

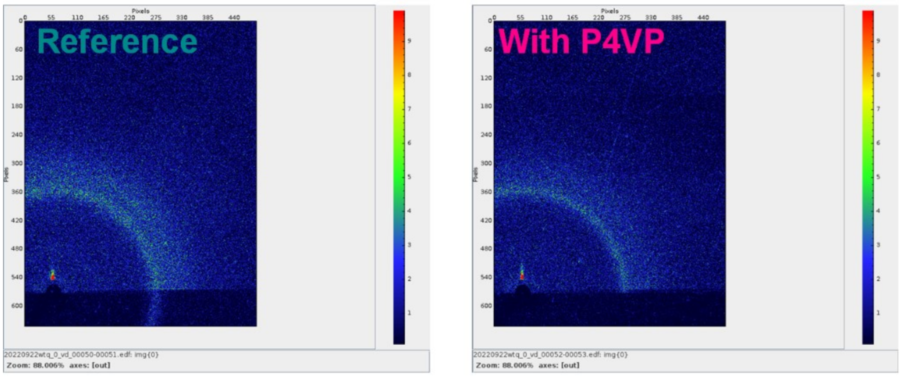

Supplementary Fig. 11 GIWAXS measurements for Spiro-OMeTAD films with and without P4VP.

As can be seen from the GIWAX plot of **Supplementary Fig. 11**, Spiro-OMeTAD has no obvious crystallization behavior with or without the addition of P4VP.

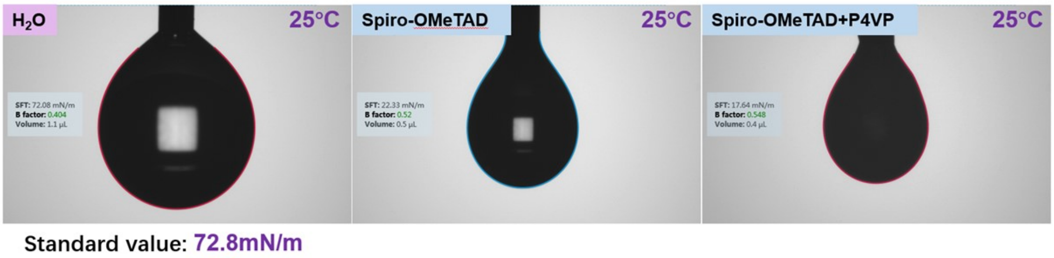

Supplementary Fig. 12 surface tension of reference and P4VP samples (Water is added to illustrate data reliability).

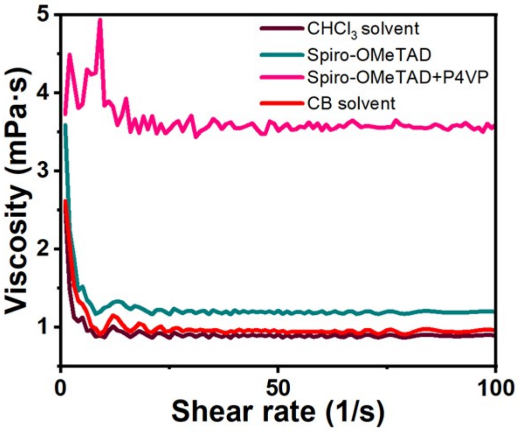

Supplementary Fig. 13 Viscosity curves of the pure CB solvent, CF solvent and the Spiro-OMeTAD solution with or without P4VP.

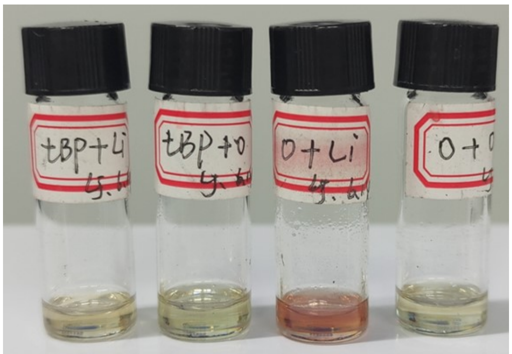

Supplementary Fig. 14 Images of Spiro-OMeTAD solutions with different additives (from left to right, Spiro-OMeTAD: tBP: LiTFSI, Spiro-OMeTAD: tBP, Spiro-OMeTAD: LiTFSI, Spiro-OMeTAD).

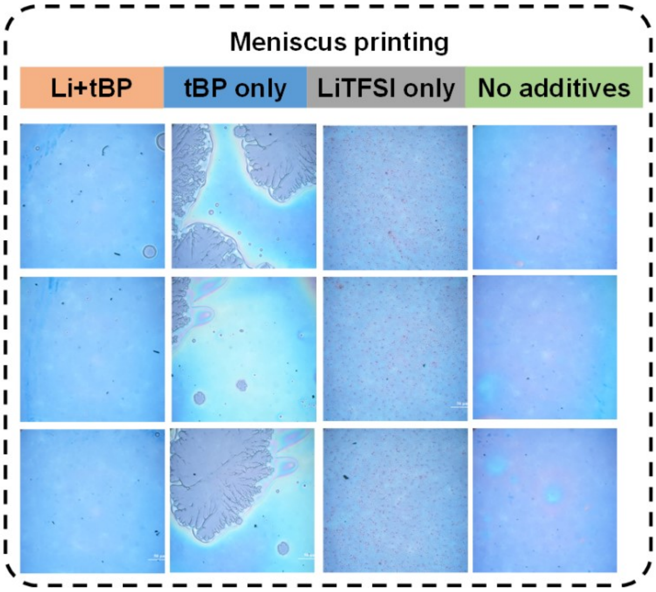

Supplementary Fig. 15 Optical microscope pictures of Spiro-OMeTAD printed with or without additives.

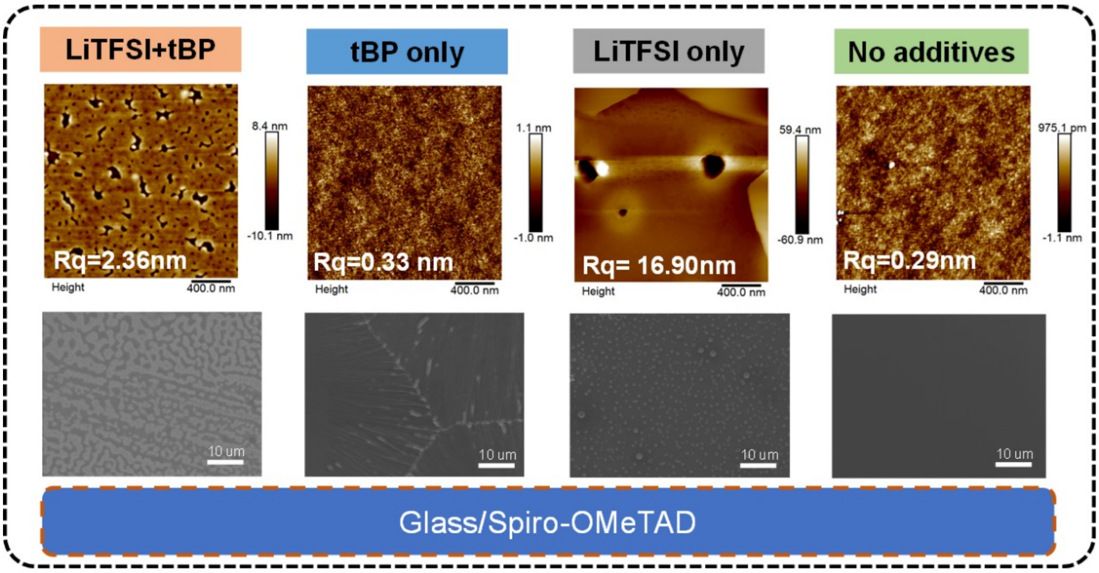

Supplementary Fig. 16 Morphology of AEM and AFM of Spiro-OMeTAD meniscus printed with or without additives.

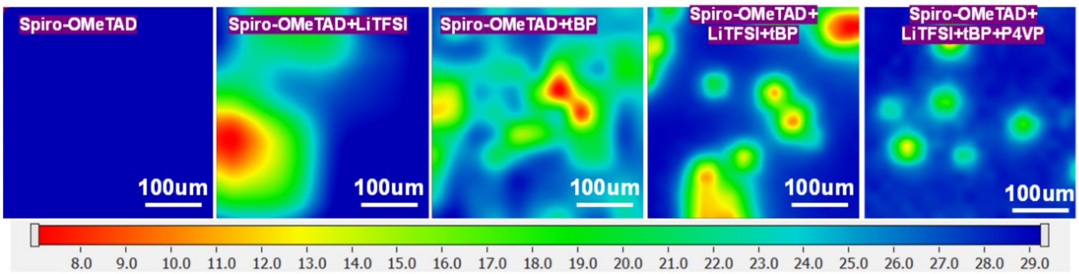

Supplementary Fig. 17 2D FTIR microscopy image of Spiro-OMeTAD.

2D FTIR microscopy is useful to characterize the effect of additives on Spiro-OMeTAD uniformity by the color change through the 1503 cm^{-1} peak height plot (Supplementary Fig. 17).[9] The results show that both LiTFSI and tBP alone lead to inhomogeneity in printed Spiro-OMeTAD. The combined effect of both exists in the presence of both. After the addition of P4VP, the printed HTL uniformity was certainly improved.

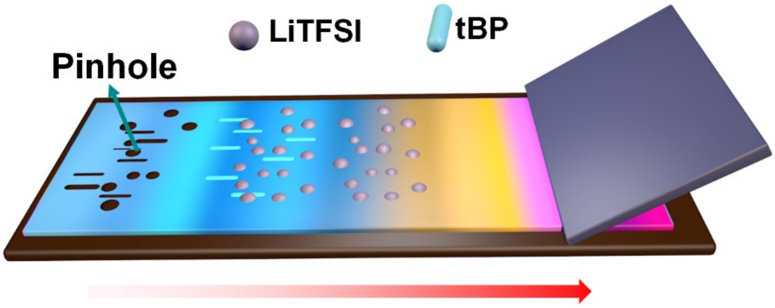

Supplementary Fig. 18 diagram of uneven printing Spiro-OMeTAD and the causes of film pinhole.

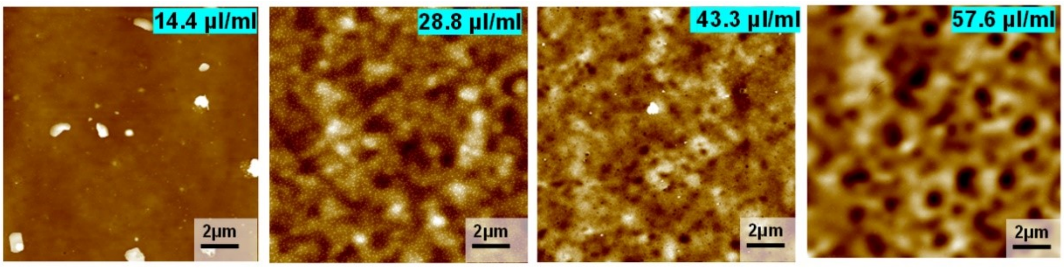

Supplementary Fig. 19 AFM images of Spiro-OMeTAD doped with different tBP concentrations.

In order to verify that the volatilization of tBP is responsible for the pore enrichment in HTLs, the spiro-OMeTAD films with gradient tBP concentrations of 14.4, 28.8, 43.3, and 57.6 μl/ml are prepared, respectively, and their micr-morphological features are performed by the atomic force microscope (AFM) measurement (Supplementary Fig. 19). It can be found that the HTLs containing 14.4 μl/ml tBP show large white particles, while the HTLs containing 28.8 μl/ml tBP seem to have a large number of small particles. In contrast, the HTLs with excessive addition of tBP (43.3 and 57.6 μl/ml) exhibit a uniform morphology, but the excessive addition of tBP always results in the disruption of the perovskite crystals, which has also been reported in previous studies [10].

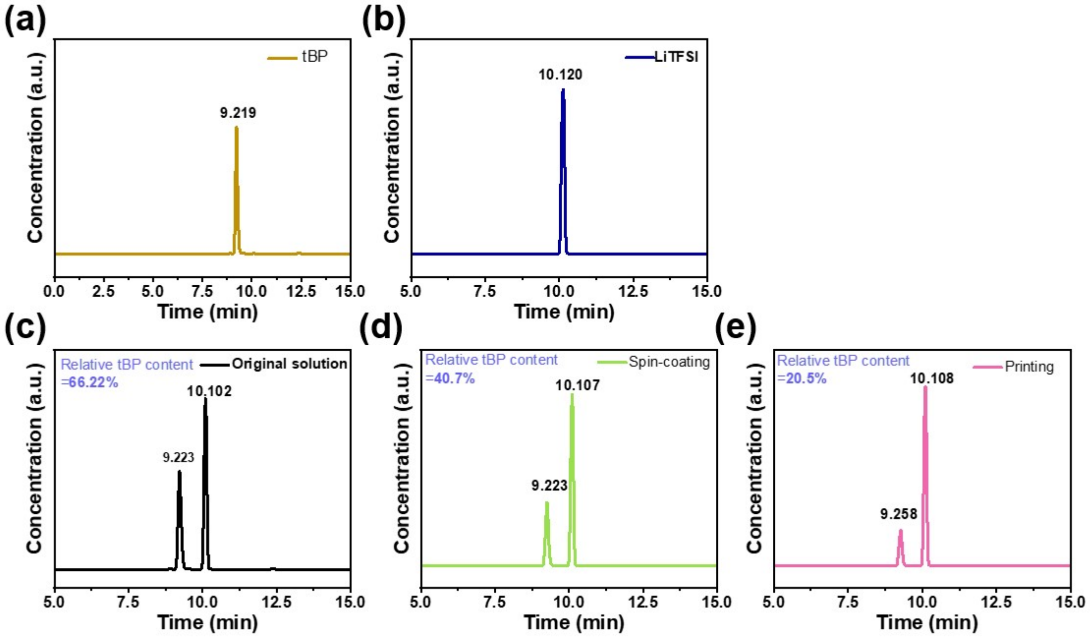

Supplementary Fig. 20 HPLC plot of pure materials and re-soluble films. (a) Pure tBP. (b)Pure LiTFSI. (c)original solution. (d) Spin-coating film. (e) Printing film.

The amount of LiTFSI and tBP in printed spiro-OMeTAD films after re-dissolution (the printed and spin-coated fresh films are redissolved in acetonitrile and then diluted in ethanol) is detected by the high-performance liquid chromatography (HPLC). Thus, the relative contents of LiTFSI and tBP obtained by HPLC can reflect the content of residual tBP in HTLs. The results demonstrate that the tBP content in the printed films is significantly lower than that in the spin-coated films and the original solution. In conclusion, we consider that the volatilization of tBP is the main reason for the appearance of holes in HTLs.

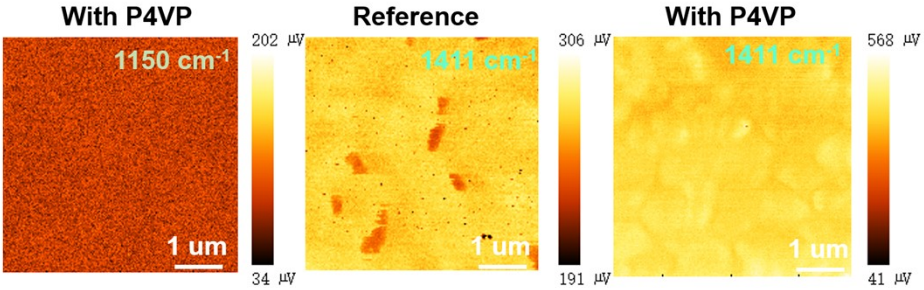

Supplementary Fig. 21 PiFM image of printed HTL with wave numbers of 1150 cm^{-1} and 1411cm^{-1}.To illustrate the distribution of LiTFSI and P4VP, higher resolution PiFM was used to illustrate this. In Supplementary Fig. 20, LiTFSI precipitation is present in the reference (the characteristic signal 1150 cm^{-1} is evident on the precipitated small particles), whereas no LiTFSI precipitation is observed in the P4VP sample, and it is difficult to observe a clear LiTFSI signal. However, tBP and P4VP are structurally similar and it is difficult to distinguish them by FITR. Using the feature 1411 cm^{-1} of tBP results in blocky shadows above the reference, while the P4VP sample stays better flattened.

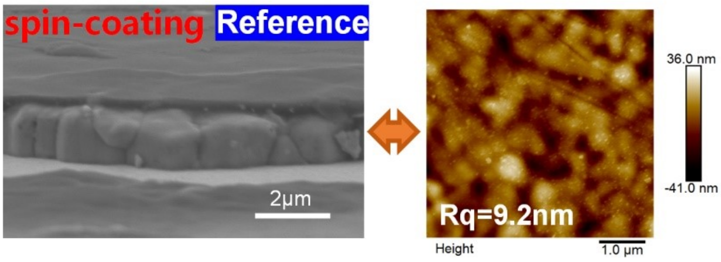

Supplementary Fig. 22 SEM section and AFM of Spiro-OMeTAD thin film prepared by spin coating process, the structure is ITO/PVK/Spiro-OMeTAD.

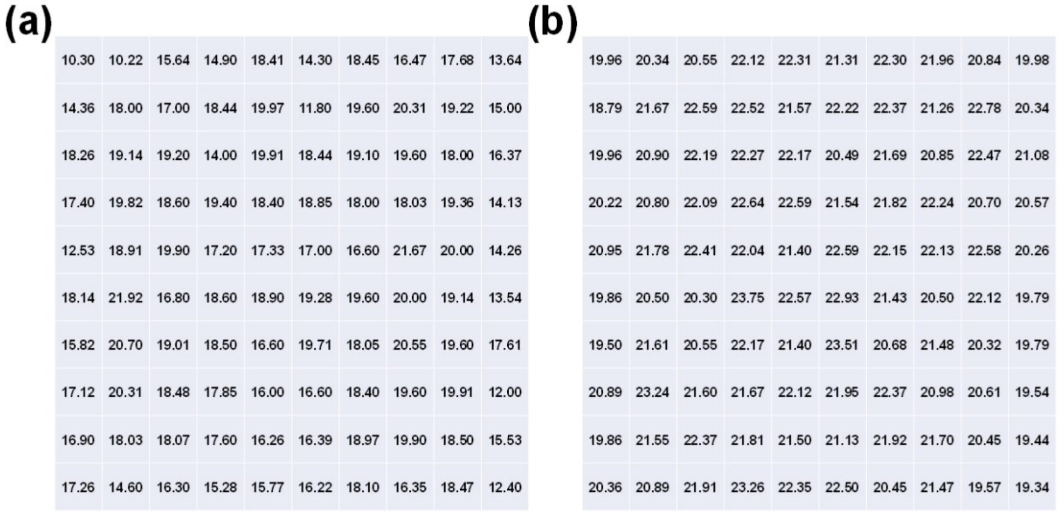

(a)

10.30	10.22	15.64	14.90	18.41	14.30	18.45	16.47	17.68	13.64
14.36	18.00	17.00	18.44	19.97	11.80	19.60	20.31	19.22	15.00
18.26	19.14	19.20	14.00	19.91	18.44	19.10	19.60	18.00	16.37
17.40	19.82	18.60	19.40	18.40	18.85	18.00	18.03	19.36	14.13
12.53	18.91	19.90	17.20	17.33	17.00	16.60	21.67	20.00	14.26
18.14	21.92	16.80	18.60	18.90	19.28	19.60	20.00	19.14	13.54
15.82	20.70	19.01	18.50	16.60	19.71	18.05	20.55	19.60	17.61
17.12	20.31	18.48	17.85	16.00	16.60	18.40	19.60	19.91	12.00
16.90	18.03	18.07	17.60	16.26	16.39	18.97	19.90	18.50	15.53
17.26	14.60	16.30	15.28	15.77	16.22	18.10	16.35	18.47	12.40

(b)

19.96	20.34	20.55	22.12	22.31	21.31	22.30	21.96	20.84	19.98
18.79	21.67	22.59	22.52	21.57	22.22	22.37	21.26	22.78	20.34
19.96	20.90	22.19	22.27	22.17	20.49	21.69	20.85	22.47	21.08
20.22	20.80	22.09	22.64	22.59	21.54	21.82	22.24	20.70	20.57
20.95	21.78	22.41	22.04	21.40	22.59	22.15	22.13	22.58	20.26
19.86	20.50	20.30	23.75	22.57	22.93	21.43	20.50	22.12	19.79
19.50	21.61	20.55	22.17	21.40	23.51	20.68	21.48	20.32	19.79
20.89	23.24	21.60	21.67	22.12	21.95	22.37	20.98	20.61	19.54
19.86	21.55	22.37	21.81	21.50	21.13	21.92	21.70	20.45	19.44
20.36	20.89	21.91	23.26	22.35	22.50	20.45	21.47	19.57	19.34

Supplementary Fig. 23 PCE data of PCE distribution of printed Spiro-OMeTAD, a) represents the reference and b) indicates the addition of P4VP. (Substrate size is 10×10 cm^2, effective area of PCE test is 0.04 cm^2).

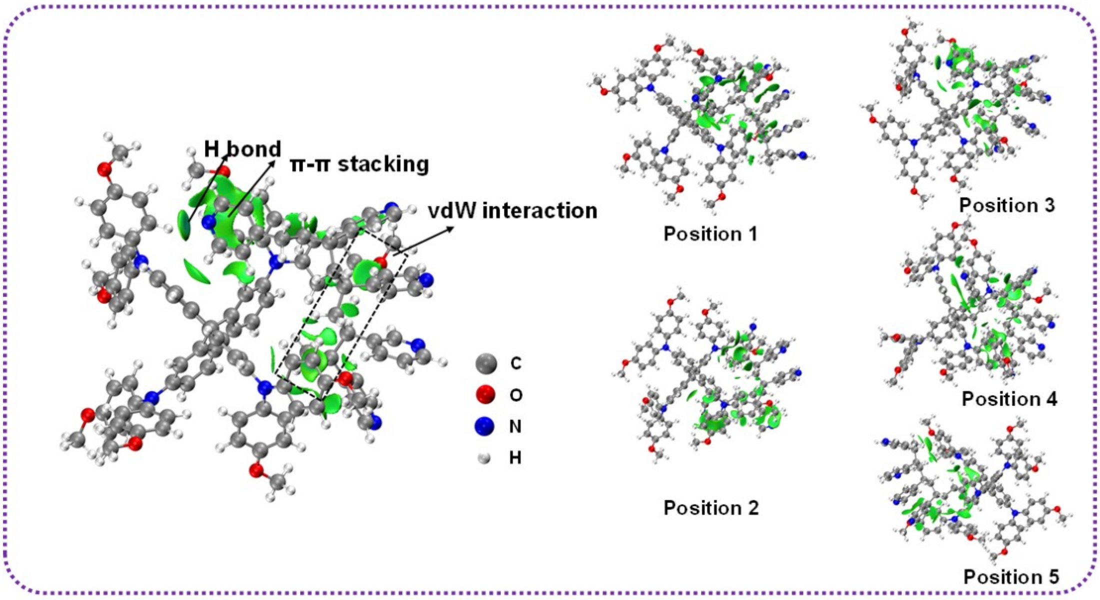

Supplementary Fig. 24 Schematic diagram of interaction between Spiro-OMeTAD molecule and P4VP molecule at different positions based on Hirshfeld partition (IGMH) (P4VP molecule is calculated by selecting five structural units).

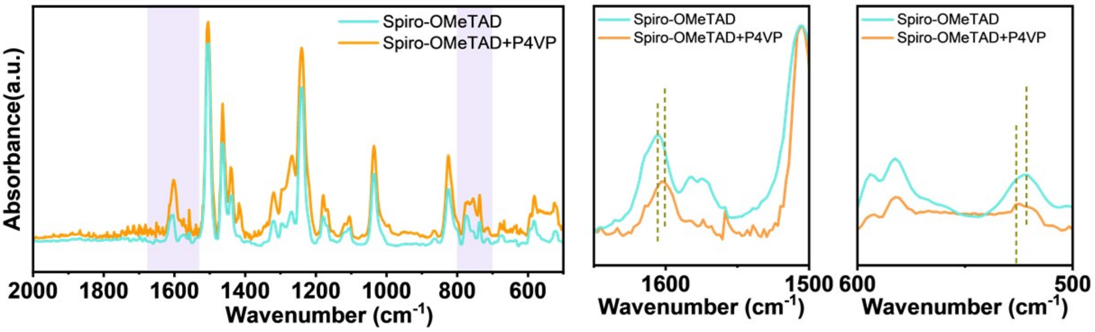

Supplementary Fig. 25 FITR spectroscopy of Spiro-OMeTAD and P4VP.

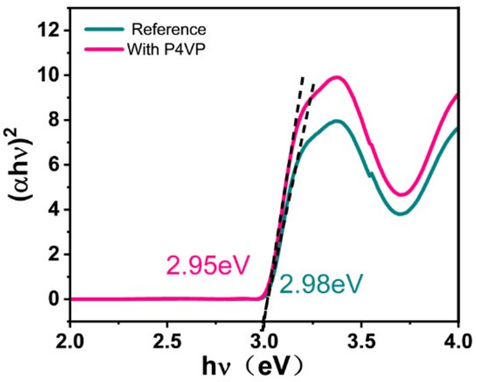

Supplementary Fig. 26 Optical band gap of Spiro-OMeTAD with and without P4VP.

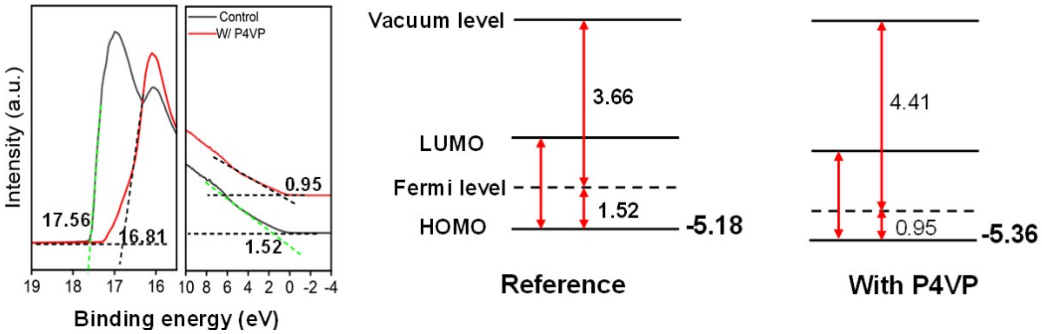

Supplementary Fig. 27 UPS measurement of Spiro-OMeTAD with or without P4VP.

As the fermi edge (E_F) of binding energy based on UPS spectra are 0, work function equation can be calculated following this equation:

$$\varphi = hv - E_{cutoff}$$

where hv is the energy of He irradiation (21.22 eV) and E_{cutoff} is secondary cutoff level

According to the UPS curve, after adding P4VP, the HOMO of Spiro-OMeTAD decreases, the Fermi level shifts to HOMO, and the work function of increases, which is beneficial to hole transport.[11]

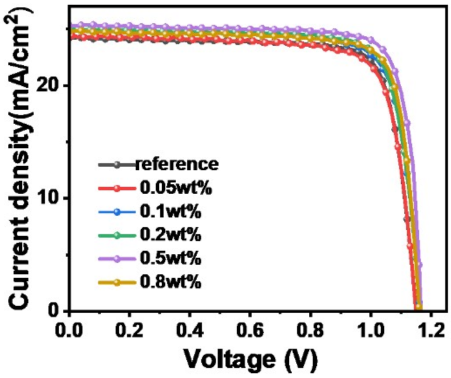

Supplementary Fig. 28 *J-V* curve with different content of P4VP.

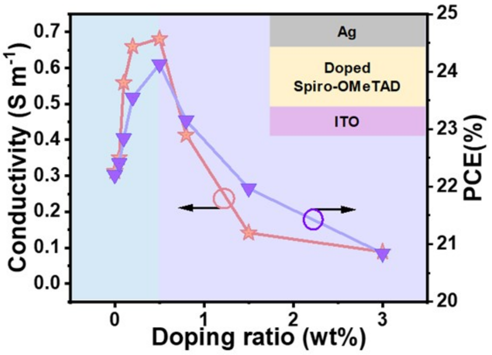

Supplementary Fig. 29 Electrical conductivity and corresponding efficiency for different P4VP doping.

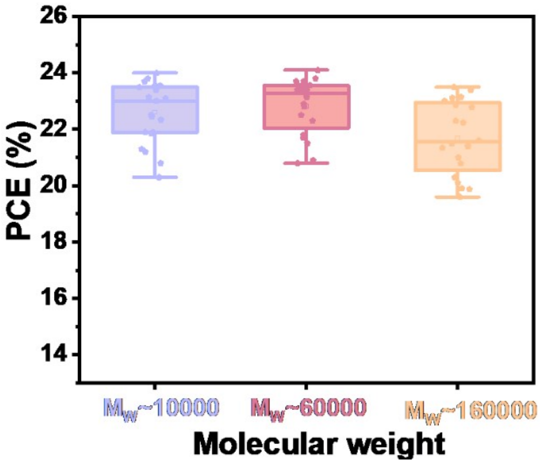

Supplementary Fig. 30 Efficiency statistics of P4VP sample with molecular weight of 10000, 60000 and 160000.

Molecular weight is an important parameter in this work, therefore, the electrical conductivity of HTLs and the PCE of PSCs under different molecular weight (M_W) conditions are summarized in **Supplementary Fig. 30**. It can be found that the P4VP molecular weights of 10000 and 60000 at the same additive content contribute similarly to the efficiency, and the difference in conductivity of the HTLs is not significant, but when the M_W reaches 160000, the efficiency starts to decrease, which is attributed to the difference in the solubility of the different molecular weights of P4VP (Usually high molecular weight implies poor solubility). In order to maximize the retention of the effect of P4VP on the rheological properties (viscosity, etc.) in the precursor, we ultimately choose the P4VP polymer with a M_W of 60000.

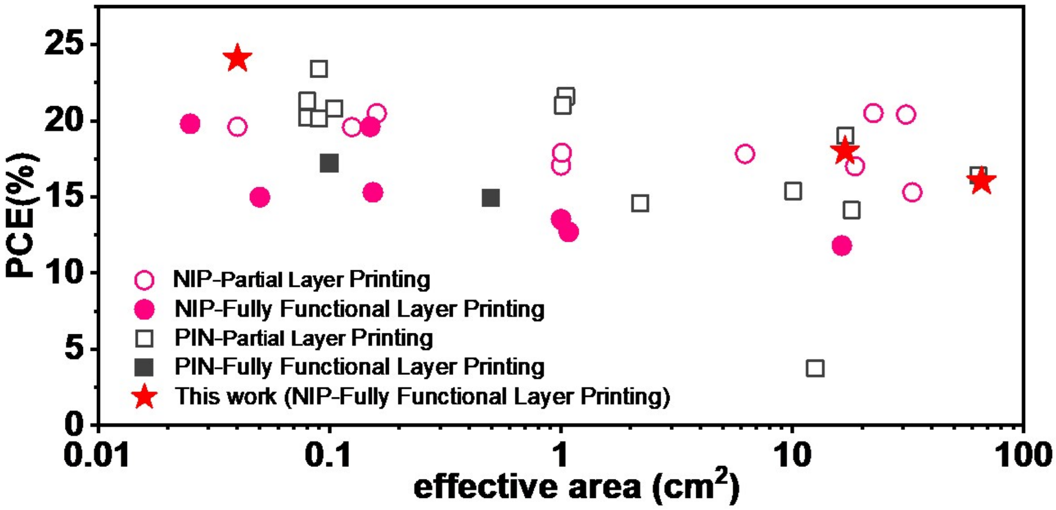

Supplementary Fig. 31 Effective area of printing work in recent years and its corresponding distribution of efficiencies (for more information see **Table S4**).

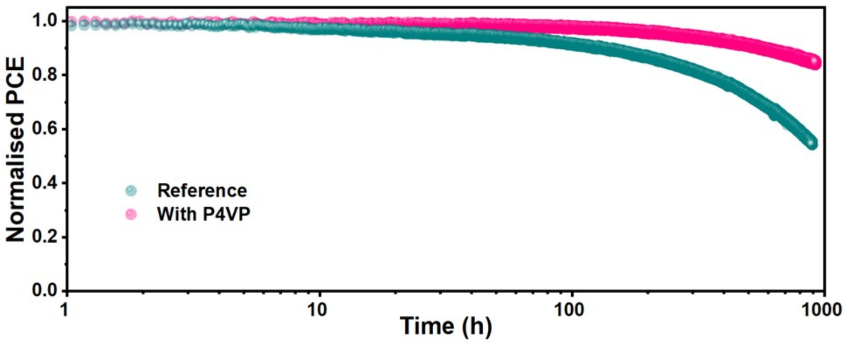

Supplementary Fig. 32 Operational stability of reference and with P4VP tracked for 940 hours.

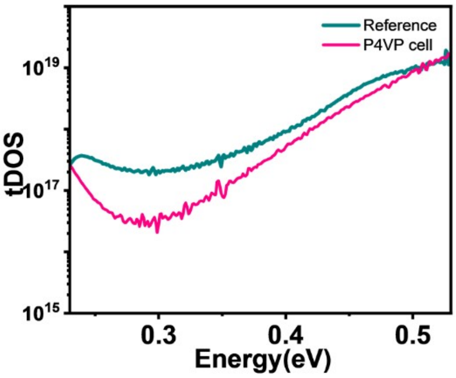

Supplementary Fig. 33 tDOS curve measured by thermal admittance spectroscopy (TAS).

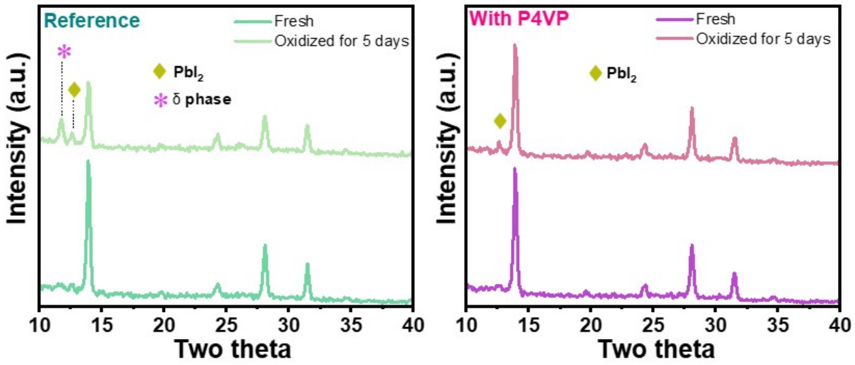

Supplementary Fig. 34 The XRD of FAPbI3 films covered with reference HTL and P4VP HTL before and after oxidation for 5 days.

First, the perovskite devices containing spiro-OMeTAD HTLs usually require an oxidation process. The presence of pinholes in the reference accelerates the attack of the perovskite crystals by moisture or oxygen during the oxidation process, which increases the defect state density of the perovskite crystals, and thus indicates the difference in SCLC curves. To verify this phenomenon, $FAPbI_3$, which is sensitive to moisture or oxygen,[12] is chosen as the photosensitive layer and covered with the HTLs. These samples are than performed to XRD characterization before and after oxidation (20 RH%) for 5 days (Supplementary Fig. 33). It can be found that the characteristic signals of PbI_2 and δ phase appear in the reference after aging, but the HTLs containing P4VP can always maintain the complete phase structure of perovskite, thus illustrating the crystal degradation of perovskite.

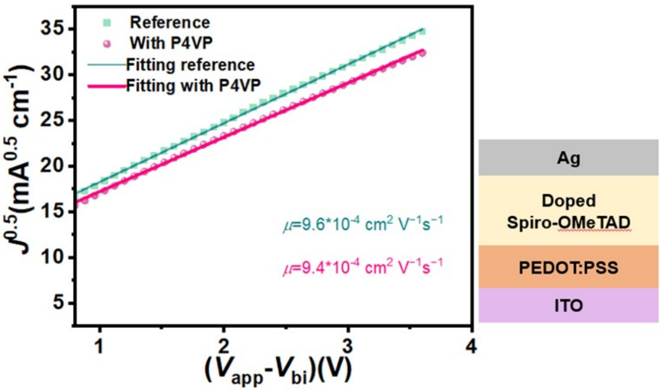

Supplementary Fig. 35 Mobility curves for reference and P4VP samples

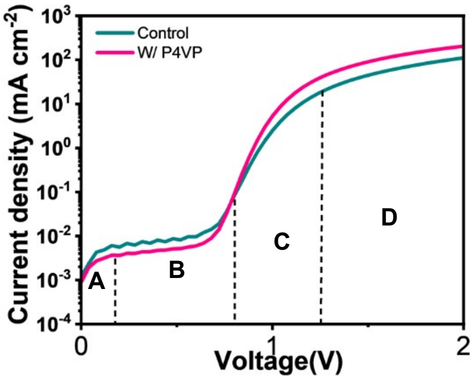

Supplementary Fig. 36 Vertical dark *J-V* curve of ITO/SnO_2/PVK/Spiro-OMeTAD/Ag.

As shown in the **Supplementary Fig. 36**, region A, B and C of the dark current curve are related to shunt current, composite current and diffusion current respectively. When the built-in potential in D region is higher than 1.2 V, the influence of composite current can be ignored. At this time, the curve is only determined by the diffusion current and limited by the series resistance (Rs) of the cell.[12]

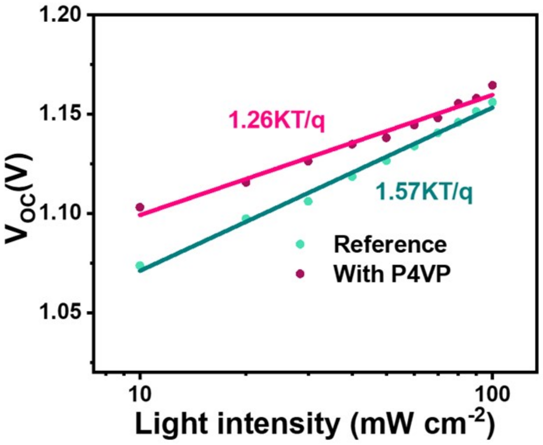

Supplementary Fig. 37 Light intensity dependence of V_{OC} of PSCs with different HTLs

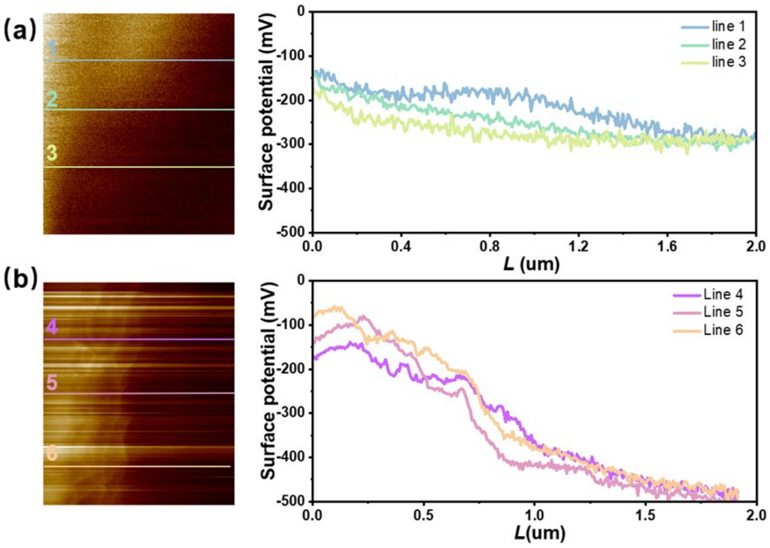

Supplementary Fig. 38 The cross-sectional KPFM images and corresponding potential difference in a line. (a)reference and (b) with P4VP

The potential transition zone between the perovskite layer and HTLs becomes clearer after introducing P4VP (Supplementary Fig. 38), while the corresponding interface in the reference exhibits an inhomogeneous transition zone, indicating that the optimized interfacial is more ordered.[13]

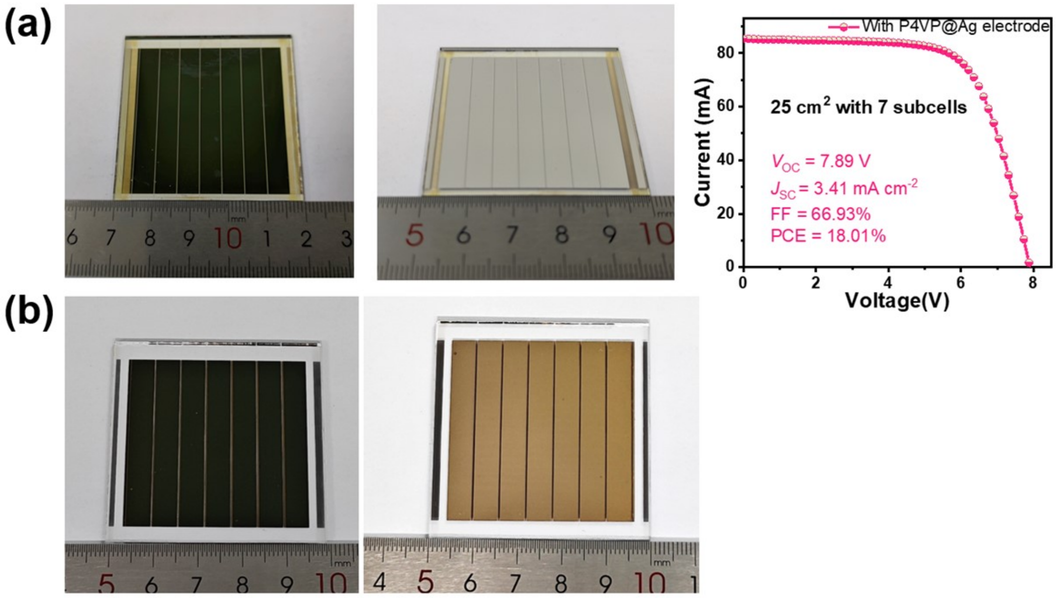

Supplementary Fig. 39 Photographs and *J*-*V* curve of 25 cm^2 PSMs. (a)Ag as the top electrode. (b) Au as the top electrode.

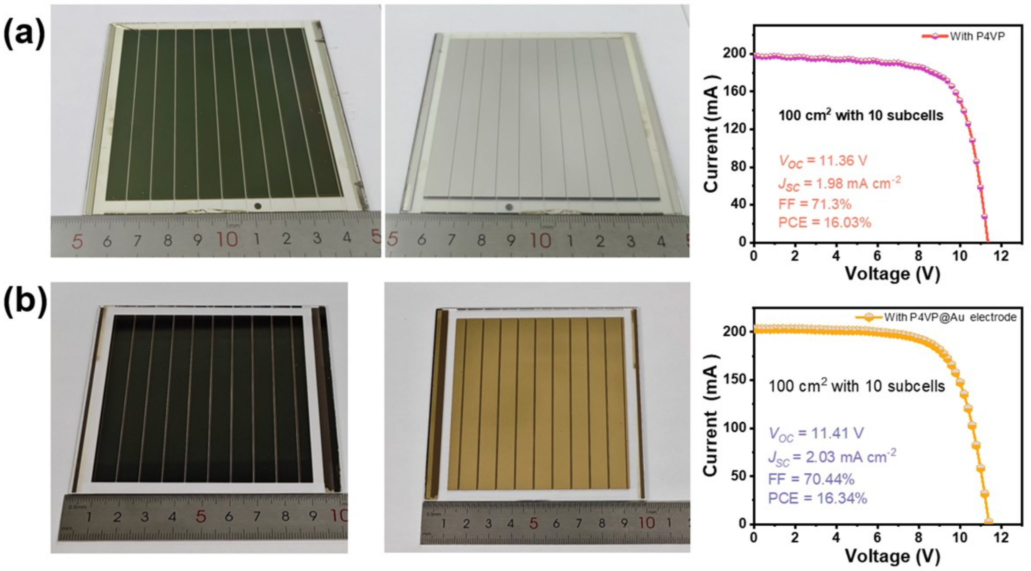

Supplementary Fig. 40 Photographs and *J-V* curve of 100 cm^2 PSMs. (a)Ag as the top electrode. (b) Au as the top electrode.

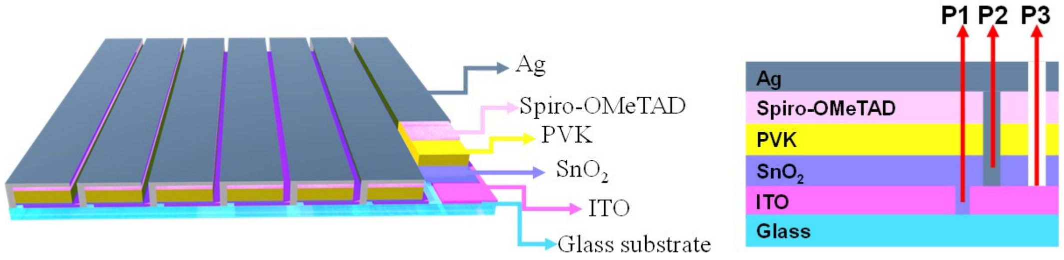

Supplementary Fig. 41 The schematic diagram of 25 cm^2 PSMs (There are seven sub-batteries) and diagram of laser etching process.

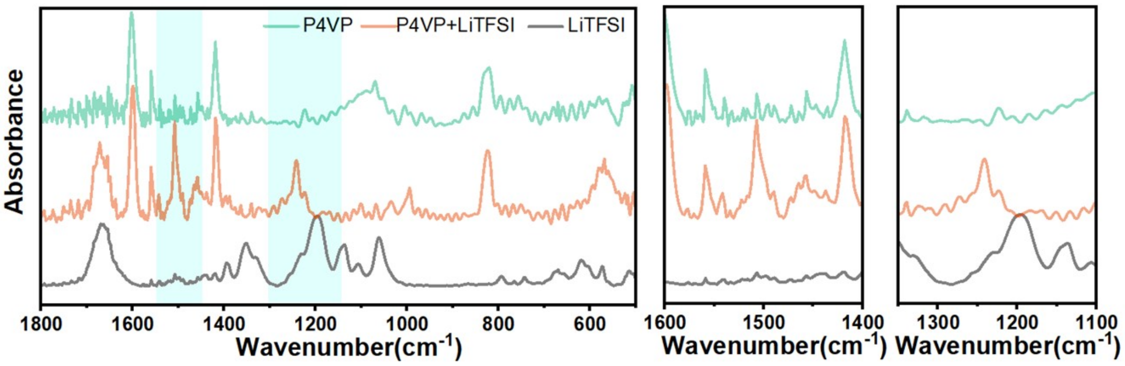

Supplementary Fig. 42 FITR spectra of LiTFSI reacted with P4VP.[14]

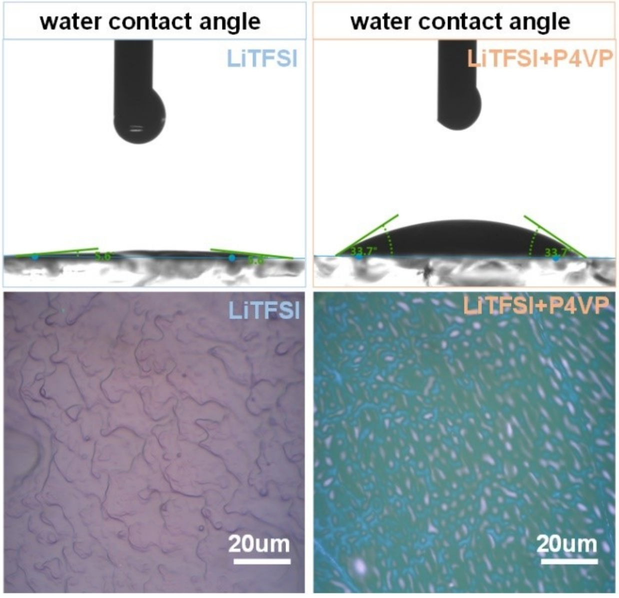

Supplementary Fig. 43 Water contact angle of LiTFSI as well as LiTFSI+P4VP and the corresponding OM diagrams.

In order to illustrate the effect of P4VP on the water uptake of LiTFSI, the pure LiTFSI and LiTFSI: P4VP films on ITO substrates are prepared and detected by the water contact angle (**Supplementary Fig. 42**). The results demonstrate that the LiTFSI is hydrophilic with a water contact angle of only about 5° or even lower, whereas the addition of P4VP increases the water contact angle to 33.7°, showing enhanced water repulsion.

Next, the optical microscope images of LiTFSI and LiTFSI: P4VP films are performed as shown in **Supplementary Fig. 42**. It can be noticed that the morphology of LiTFSI and LiTFSI: P4VP on the substrate is completely different, and we speculate that the enhanced water resistance is due to the binding of the pyridine terminus in P4VP to Li^+, which exposes the alkyl chains on the film surface and improves the hydrophobicity of HTLs.

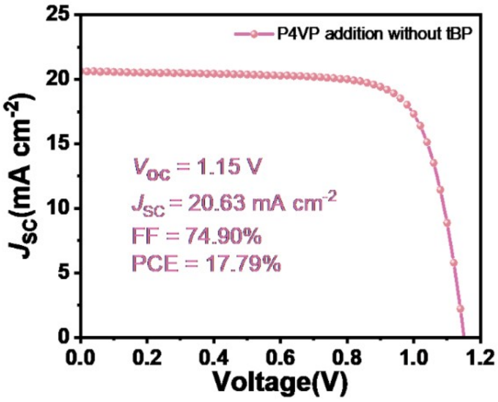

Supplementary Fig. 44 *J-V* curvy of Spiro-OMeTAD without tBP.

When P4VP completely replaces tBP, the current density and the fill factor are drastically reduced, which leads to a significant decrease in the efficiency of perovskite devices.

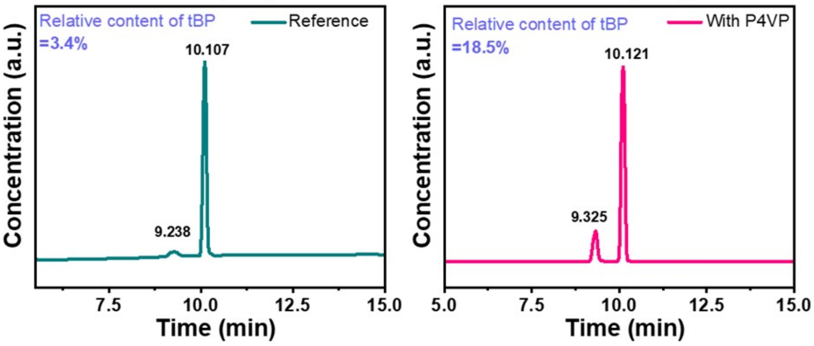

Supplementary Fig. 45 HPLC characterization of reference and P4VP sample powder dissolve in acetonitrile (The powder is obtained by evaporating corresponding solution, then it is dissolved in acetonitrile and finally filtered Spiro-OMeTAD).

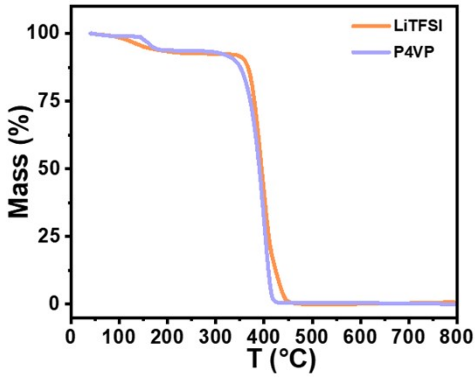

Supplementary Fig. 46 TGA curves of pure LiTFSI and pure P4VP.

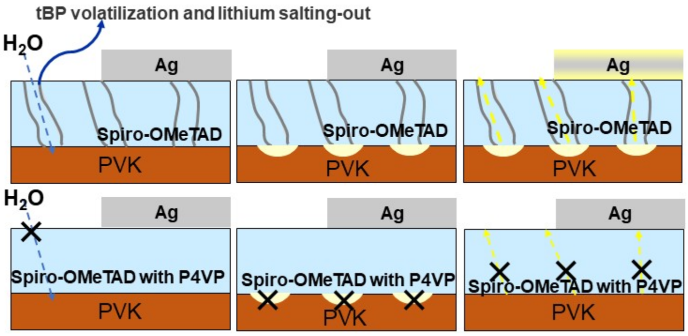

Supplementary Fig. 47 Diagrammatic representation of the mechanism of Spiro-OMeTAD destruction leading to corrosion of perovskite by water.

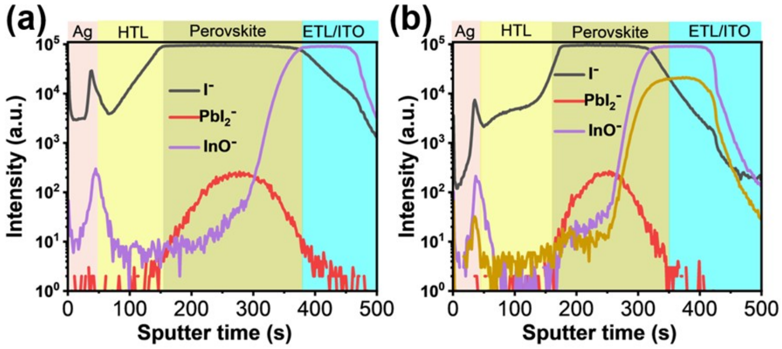

Supplementary Fig. 48 TOF-SIMS elemental depth profiles of devices based on (a) reference and (b) with P4VP (Anionic mode).

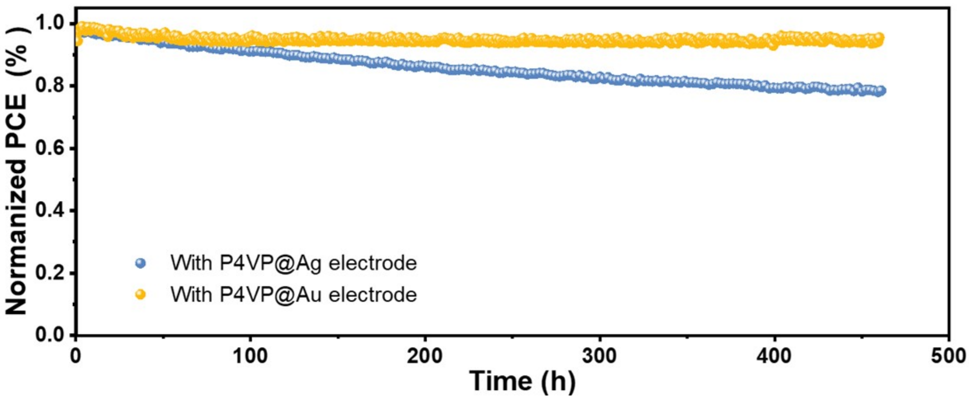

Supplementary Fig. 49 PCE track of the 100 cm^2 PSMs with different electrode under simulated sunlight (AM 1 5G, 100 mW cm^{-2}) at room temperature.

Table S1 Saturated vapor pressure and boiling point of the solvent chlorobenzene and chloroform.

	saturated vapor pressure （kPa） （25 °C）	boiling point (°C)
CB	1.17	131.7
$CHCl_3$	21.2	61.3

The saturated vapor pressure of $CHCl_3$ is much lower than that of CB,[15] representing a faster evaporation rate, and according to the theory of meniscus printing,[16, 17]it is easier to achieve uniform film formation.

Table S2 Binding energy data for molecules at the lowest binding energy position when performing simulations using molecular dynamics as well as DFT.

Position	A[a)] Hartee	B[b)] Hartee	AB[c)] Hartee	E_{ads}[d)] Hartee	E_{ads} kcal/mol
1	-1590.6142	-3948.7048	-5539.3916	-0.0725	-45.5191
2	-1590.6142	-3948.7048	-5539.3992	-0.0801	-50.2859
3	-1590.6142	-3948.7048	-5539.3979	-0.0788	-49.46862
4	-1590.6142	-3948.7048	-5539.3919	-0.0728	-45.70619
5	-1590.6142	-3948.7048	-5539.3963	-0.0772	-48.44609
6	-1590.6142	-3948.7048	-5539.3904	-0.0713	-44.77202

[a)]Column A represents the free energy of polytetraethylene pyridine (5 structural units); [b)] Column B represents the free energy of Spiro-OMeTAD; [c)] Column AB is the energy of combining two molecules; [d)] its E_{ads} (binding energy) can be calculated according to the formula of $E_{ads}=E_{AB}-E_{A}-E_{B}$. (1-6 respectively represent the positions with the lowest energy calculated by molecular dynamics simulation.)

Table S3 Electrical parameters of *J-V* curve with different content of P4VP

	V_{oc} (V)	J_{sc} (mA/cm^2)	*FF* (%)	PCE (%)
0	1.15	24.21	79.76	22.2
0.05wt%	1.15	24.69	78.94	22.41
0.10wt%	1.16	24.87	79.17	22.84
0.20wt%	1.17	25.13	80.07	23.55
0.50wt%	1.16	25.33	81.72	24.13
0.80wt%	1.16	24.84	80.12	23.15

Table S4 A summary of the printing work in recent years, mainly including its main printing methods, printed layers as well as the effective area and its structure, and corresponding photovoltaic conversion efficiency (this table only counts the efficiency of rigid devices).

Printing method	effective area (cm^2)	Printed layer	PCE (%)	Structure	Literature cited
blade coating	17	PVK	19	p-i-n	Adv. Energy Mater., **2022**, 12, 2102820
blade coating	1	TiO2, PVK	17.06	n-i-p	Joule, **2018**, 18, 1313-1330
blade coating	22.4	PVK	20.5	n-i-p	Nat. Energy, **2022**,7, 528–536
		SnO_2 (CBD), PVK, Spiro-OMeTAD	16.2	n-i-p	Nature**, 2022,** 12, 266–271
screen printing	0.05	SnO2, PVK, Spiro-OMeTAD	14.98	n-i-p	
	1	SnO2, PVK, Spiro-OMeTAD	13.53	n-i-p	
	16.37	SnO2, PVK, Spiro-OMeTAD	11.8	n-i-p	
blade coating	0.150	SnO2, PVK, Spiro-OMeTAD	19.6	n-i-p	ACS Energy Lett., **2018**, 3, 10, 2558–2565
blade coating	0.5	PTAA, PVK, PCBM, BCP	14.9	p-i-n	Nano. Res., **2021**, 14, 1034–1042
blade coating	63.7	PTAA, PVK	16.4	p-i-n	Sci. Adv., **2019**, 5, eaax7537
	0.08	PTAA, PVK	21.3	p-i-n	
blade coating	33	PTAA, PVK	15,3	n-i-p	Nat. Energy, **2018**, 3, 560–566
inkjet printing	1.05	PVK	21.6	p-i-n	Adv. Energy Mater., **2020**, 10, 1903184
inkjet printing	0.04	PVK	19.6	n-i-p	ACS Appl. Mater. Interfaces, **2020**, 12, 39082−39091
inkjet printing	1.01	PVK	17.9	n-i-p	
inkjet printing	0.1	NiO_X, PVK, PCBM, BCP	17.2	p-i-n	Adv. Mater. Technol., **2021**, 6, 2000271

blade coating	0.08	PVK	20.2	p-i-n	Nat. Commun., **2018**, 9, 1625
blade coating	0.09	PVK	20.14	p-i-n	Adv. Energy Mater., **2020**, 10, 2000173
	10.08	PVK	15.38		
D-bar	0.125	PVK	19.58	n-i-p	J. Mater. Chem. A, **2020**, 8, 9345-9354
D-bar	18.66	PVK	17.01	n-i-p	J. Mater. Chem. A, **2020**, 8, 9345-9354
blade coating	0.16	PVK, SnO_2(CBD)	20.49	n-i-p	J. Mater. Chem. A, **2020**, 8, 8447-8454
blade printing	18	PVK	14.13	p-i-n	Nano. Research Energy, **2022**, 1, 9120004.
slot die	2.2	2PACZ, PVK,	14.57	p-i-n	Adv. Energy Mater.**2021**, 11, 2003460
	12.56	2PACZ, PVK,	3.73	p-i-n	
	0.105	2PACZ, PVK,	20.8	p-i-n	
D-bar	6.25	PVK	17.82	n-i-p	ACS Energy Lett. **2019**, 4, 1189–1195
spraying	1.08	PVK, SnO2, Spiro-OMeTAD	12.7	n-i-p	Sci. Rep. **2020**, 10, 6610.
	0.154	PVK, SnO2, Spiro-OMeTAD	15.3	n-i-p	
	0.025	PVK, SnO2, Spiro-OMeTAD	19.8	n-i-p	
D-bar	31	PVK	20.4	n-i-p	Joule, **2021**, 5, 2420–2436
spin coating	1.02	--	21.0	p-i-n	Adv. Mater., **2023**, 23, 01752
slot die	0.09	PVK	23.4	p-i-n	Joule, **2022**, 6, 1931–1943
	174	PVK	18.6	p-i-n	
blade printing	0.04	PVK, SnO2, Spiro-OMeTAD	24.1	n-i-p	This work

16.9	PVK， SnO2, Spiro-OMeTAD	18.16	n-i-p	This work
65.7	PVK， SnO2, Spiro-OMeTAD	16.34	n-i-p	This work

Reference

1. C. Bannwarth, E. Caldeweyher, S. Ehlert, A. Hansen, P. Pracht, J. Seibert, S. Spicher and S. Grimme, *WIREs Computational Molecular Science*, 2020, **11**, e1493.
2. Tian Lu, Molclus program, Version 1.9.9.9, http://www.keinsci.com/research/molclus.html (accessed Dec 19, 2022).
3. A. D. Becke, *Journal of Chemical Physics*, 1993, **98**, 1372-1377.
4. P. J. Stephens, F. J. Devlin, C. F. Chabalowski and M. J. Frisch, *The Journal of Physical Chemistry*, 1994, **98**, 11623-11627.
5. W. J. Hehre, R. Ditchfield and J. A. Pople, *Journal of Chemical Physics*, 1972, **56**, 2257-2261.
6. T. Lu and Q. Chen, *J Comput Chem*, 2022, **43**, 539-555.
7. W. Humphrey, A. Dalke and K. Schulten, *Journal of Molecular Graphics*, 1996, **14**, 33-38.
8. T. Lu and F. Chen, *J Comput Chem*, 2012, **33**, 580-592.
9. E. J. Juarez-Perez, M. R. Leyden, S. Wang, L. K. Ono, Z. Hawash and Y. Qi, *Chemistry of Materials*, 2016, **28**, 5702-5709.
10. S. Wang, Z. Huang, X. Wang, Y. Li, M. Günther, S. Valenzuela, P. Parikh, A. Cabreros, W. Xiong and Y. S. J. J. o. t. A. C. S. Meng, 2018, **140**, 16720-16730.
11. Q. Chen, J. Wu, X. Wang, G. Li, Z. Song, Y. Xu, C. Deng, Y. D. W. Sun and Z. J. C. E. J. Lan, 2022, **450**, 138313.
12. Y. Qi, M. Almtiri, H. Giri, S. Jha, G. Ma, A. K. Shaik, Q. Zhang, N. Pradhan, X. Gu and N. I. J. A. E. M. Hammer, 2022, **12**, 2202713.
13. L. Xiao, X. Xu, Z. Lu, J. Zhao, R. Liu, Y. Ye, R. Tang, W.-Q. Liao, R.-G. Xiong and G. J. N. E. Zou, 2023, **107**, 108114.
14. S. G. Kim, T. H. Le, T. de Monfreid, F. Goubard, T. T. Bui and N. G. J. A. M. Park, 2021, **33**, 2007431.
15. D. Zheng, J. Huang, Y. Zheng and J. J. O. E. Yu, 2015, **25**, 275-282.
16. Y. Yang, Y. Wang, Z. Qu, K. Zhang, T. Liang, S. Chen, W. Lv, F. Min, Y. Chen and Y. J. A. C. Qiao, 2023, **135**, e202300971.
17. R. Ma, T. Yang, Y. Xiao, T. Liu, G. Zhang, Z. Luo, G. Li, X. Lu, H. Yan, B. J. E. Tang and E. Materials, 2022, **5**, 977-985.